Computational Modeling of Failure Processes in Polymers

van der Giessen, Erik; Estevez, R.; Pijnenburg, K.G.W.; Tijssens, M.G.A.

Published in:
EPRINTS-BOOK-TITLE

Publication date:
1999

ECCM '99
European Conference on
Computational Mechanics
August 31 – September 3
München, Germany

COMPUTATIONAL MODELING OF FAILURE PROCESSES IN POLYMERS

E. Van der Giessen, R. Estevez, K.G.W. Pijnenburg and M.G.A. Tijssens
Koiter Institute Delft
Delft University of Technology, The Netherlands
e–mail: E.vanderGiessen@wbmt.tudelft.nl

Key words: Micromechanics, fracture, polymers, viscoplasticity, crazing, shear bands

Abstract. *This paper deals with the modeling of the key mechanisms involved in the fracture of polymers: shear yielding and crazing. Along with the continuum model for shear yielding, we will discuss a recently proposed cohesive surface model for crazing. Applications to be presented include the study of the competition between the two mechanisms during growth of a mode I crack, and a numerical investigation of the role of localized deformations in failure of a polymer blend.*

1 Introduction

The materials literature on polymer behavior (e.g. [1]) usually recognizes two mechanisms for failure: shear yielding and crazing. Shear yielding is what the solid mechanics community refers to as plasticity, while crazing is a peculiar brittle failure mechanism of macromolecular materials. Most solid polymers, such as polymethylmethacrylate (PMMA) or plexiglass and polycarbonate (PC), can exhibit both mechanisms, depending on stress state, temperature, strain rate and other factors. Under tension, most polymers fracture in a brittle manner by crazing, but even PMMA can be made to deform to strains on the order of 100% when crazing can be suppressed. The competition between the two governs the brittle-ductile transition.

There has been much research devoted to the study of the two mechanisms; from a molecular perspective by polymer materials scientists, and from an application point of view by engineers. Though this has provided a lot of information on both sides of the spectrum, the link between molecular characteristics and engineering properties are still largely unexplored. It is only quite recently that this gap is beginning to be bridged using similar micromechanical modeling techniques that have been successful in the study of metal fracture. This paper gives an overview of recent computational work dealing with two important issues in polymer fracture.

The first part addresses some basic issues in the competition between plasticity (by shear yielding) and crazing. Shear yielding is described here by a micromechanically-motivated continuum model which captures the key characteristics of large strain plastic flow, namely rate and temperature yield followed immediately by intrinsic strain softening and followed by anisotropic re-hardening at continued plastic deformation (e.g. [2]). Then, we demonstrate how crazing can be modeled using the concept of cohesive surfaces. The constitutive response, in terms of the traction-separation law, incorporates the stress-state dependent initiation of crazing, the rate-dependent widening of a craze caused by fibrillation as well as the final breakdown of crazes. One of the examples shows how crazing and plasticity interact near the tip of an existing crack under mode I loading conditions [3]. In this finite element model, a single cohesive surface is laid out in front of the crack. A second application employs cohesive surface elements immersed throughout the continuum elements in order to study the development of crazing around a hole in a plastic plate [4].

In the second part, we consider failure of polymer-rubber blends. These typically consist of a brittle matrix and a dispersion of small rubber particles, which are intended to toughen the material. The toughening relies on the internal cavitation of the rubber particles, which is commonly believed to relieve the stress triaxiality so as to favor shear yielding over crazing of the matrix [5]. We summarize the findings of a number of computational studies into these phenomena [6, 7, 8]. The role of the initiation and propagation of shear bands in between the particles will be highlighted [6]. We will also show how massive shear banding in between the cavitated particles governs the macroscopic behavior [8].

2 Viscoplastic flow in amorphous polymers

Plastic deformation is usually referred to as 'shear yielding' in the polymer community, which is suggestive of the geometry of this deformation mechanism. The constitutive model that we have adopted for it in all studies to be discussed later, is partly a phenomenological model and partly based on micromechanical considerations. The original ideas in a one-dimensional context date back to the 60's, while the basis for the three-dimensional (3-D) theory was given by Boyce *et al.* [9]. The specific theory to be used here though involves a number of modifications, which have evolved over a number of years and has been summarized in [10].

2.1 Constitutive Model

The constitutive model is conveniently formulated in terms of the Cauchy stress tensor $\boldsymbol{\sigma}$ and the conjugate rate of deformation tensor $\boldsymbol{D}$. The latter is the symmetric part of the velocity gradient tensor $\boldsymbol{L} = \dot{\boldsymbol{F}}\boldsymbol{F}^{-1}$, $\boldsymbol{D} = \frac{1}{2}(\boldsymbol{L} + \boldsymbol{L}^{\mathrm{T}})$, $\boldsymbol{W} = \frac{1}{2}(\boldsymbol{L} - \boldsymbol{L}^{\mathrm{T}})$, $\boldsymbol{F}$ being the deformation gradient tensor. The model is based on the usual split of $\boldsymbol{D}$ into a thermoelastic part $\boldsymbol{D}^{\mathrm{e}}$ and an inelastic part $\boldsymbol{D}^{\mathrm{p}}$,

$$\boldsymbol{D} = \boldsymbol{D}^{\mathrm{e}} + \boldsymbol{D}^{\mathrm{p}} \,. \tag{1}$$

Thermal effects will not be considered in any of the examples to be presented later, so that $\boldsymbol{D}^{\mathrm{e}}$ only governs the elastic behavior. Assuming the elastic strains to remain small, the elastic part of the response is taken to be governed by

$$\overset{\nabla}{\boldsymbol{\sigma}} = \boldsymbol{\mathcal{L}}^{\mathrm{e}}\boldsymbol{D}^{\mathrm{e}} \,, \tag{2}$$

where $\boldsymbol{\mathcal{L}}^{\mathrm{e}}$ is the standard fourth-order isotropic elastic modulus tensor in terms of the Young's modulus E and Poisson's ratio ν. Furthermore, $\overset{\nabla}{\boldsymbol{\sigma}} = \dot{\boldsymbol{\sigma}} - \boldsymbol{W}\boldsymbol{\sigma} + \boldsymbol{\sigma}\boldsymbol{W}$ is the Jaumann derivative of Cauchy stress based on the continuum spin tensor $\boldsymbol{W}$.

The constitutive formulation for $\boldsymbol{D}^{\mathrm{p}}$ is based on the idea to represent the inelastic deformation process by a parallel combination of a viscoplastic yield element and a hardening element. Postponing the physical interpretations of these two for a moment, this idea leads to introducing in 3-D of a back stress tensor $\boldsymbol{b}$, so that the difference $\bar{\boldsymbol{\sigma}} = \boldsymbol{\sigma} - \boldsymbol{b}$ is the driving stress for yield. Assuming that the corresponding yield response is isotropic and isochoric, the inelastic strain rate tensor $\boldsymbol{D}^{\mathrm{p}}$ can be written as [1]

$$\boldsymbol{D}^{\mathrm{p}} = \frac{\dot{\gamma}^{\mathrm{p}}}{\sqrt{2}\,\tau}\bar{\boldsymbol{\sigma}}' \,; \quad \tau = \sqrt{\tfrac{1}{2}\bar{\boldsymbol{\sigma}}' \cdot \bar{\boldsymbol{\sigma}}'} \,, \quad \dot{\gamma}^{\mathrm{p}} = \sqrt{\boldsymbol{D}^{\mathrm{p}} \cdot \boldsymbol{D}^{\mathrm{p}}} \,, \tag{3}$$

τ and $\dot{\gamma}^{\mathrm{p}}$ being the equivalent shear stress and equivalent inelastic shear rate, respectively, so that the energy dissipation rate per unit volume is given by

$$\bar{\boldsymbol{\sigma}}' \cdot \boldsymbol{D}^{\mathrm{p}} = \sqrt{2}\,\tau\dot{\gamma}^{\mathrm{p}} \,. \tag{4}$$

[1] The factor $\sqrt{2}$ in (3) and (4) is a consequence of the definition of $\dot{\gamma}^{\mathrm{p}}$ [see (3)] that was originally used [9] and which is maintained here for consistency.

Completion of the constitutive model requires specification of $\dot{\gamma}^{\mathrm{p}}(\tau)$ and a constitutive equation for the back stress $\boldsymbol{b}$.

Although the physical understanding of yield in amorphous is still rather limited, there are a number of theories in the literature. The one we have used is based on a theory by Argon [11] which leads to the following expression for the plastic shear rate:

$$\dot{\gamma}^{\mathrm{p}} = \dot{\gamma}_0 \exp\left[-\frac{As}{T}\left(1-\left(\frac{\tau}{s}\right)^{5/6}\right)\right] . \tag{5}$$

Here, $\dot{\gamma}_0$ and A are material parameters, and s is the shear strength, which is specified in Argon's original theory in terms of the elastic molecular properties but which is considered here as a separate material parameter. Even though plastic flow in amorphous polymers does not lead to a significant plastic dilatation, the yield stress is known to be *pressure sensitive* in a linear manner for many glassy polymers. This is incorporated in (5) by replacing s with $s+\alpha p$, where α is the pressure sensitivity coefficient.

There is conclusive experimental evidence that glassy polymers exhibit *intrinsic strain softening* upon yield. As the physical mechanisms are not yet understood well, we adopt a purely phenomenological description of softening ([9]) in which s in (5) is taken to evolve from the initial value s_0 with plastic strain according to the first-order evolution law

$$\dot{s} = h(1-s/s_{\mathrm{ss}})\dot{\gamma}^{\mathrm{p}} , \tag{6}$$

in which h is an additional material parameter and s_{ss} is the final, steady-state value. It is known that the softening in most polymers depends on temperature and, to a lesser extent, on strain-rate, but there have only been few attempts to capture these effects (e.g. [12]). Since we shall consider only isothermal processes here, and within a limited range of strain-rates, we make no attempt here to account for these effects.

The *strain hardening* in amorphous polymers is due to the stretching of their network-like molecular structure during plastic flow. This network is usually regarded to be due to physical entanglements of the long molecular chains. Thus, it bears a definite resemblance to the network structure of rubbers even though the nodes are formed then by chemical cross-links. Plastic stretching of the entanglement network leads to the gradual alignment of the molecular chains along the principal plastic stretch direction, accompanied by a reduction of the entropy of the network; this is referred to as *orientational hardening*. In the 3-D theory [9], the back stress tensor $\boldsymbol{b}$ is thus taken to be determined by the accumulated plastic stretch tensor $\boldsymbol{V}^{\mathrm{p}}$, through its principal components b_α with respect to the unit principal directions $\boldsymbol{e}^{\mathrm{p}}_\alpha$, [2]

$$\boldsymbol{b} = \sum_\alpha b_\alpha(\boldsymbol{e}^{\mathrm{p}}_\alpha \otimes \boldsymbol{e}^{\mathrm{p}}_\alpha) . \tag{7}$$

The principal components are taken to be direct functions of the principal plastic stretches. In what follows, we shall assume that the elastic strains remain small enough to allow the plastic

[2] To avoid confusion, principal tensor components and the corresponding eigenvectors are denoted with Greek indices, for which the summation convention is not implied

stretch tensor $\boldsymbol{V}^{\mathrm{p}}$ to be approximated as $\boldsymbol{V}^{\mathrm{p}} \approx \boldsymbol{B}^{1/2}$, where $\boldsymbol{B} = \boldsymbol{F}\boldsymbol{F}^{\mathrm{T}}$ is the left Cauchy-Green tensor.

Various rubber theories are available for implementation in (7), including the physically motivated Gaussian network theory or the more refined non-Gaussian theory [13]. Wu and Van der Giessen [2] developed a model that accounts for the fully 3-D orientation distribution of molecular chains in a network. Furthermore, they showed that their numerical results are captured to high accuracy by

$$\boldsymbol{b} = (1-\rho)\boldsymbol{b}^{3-\mathrm{ch}} + \rho\boldsymbol{b}^{8-\mathrm{ch}}\,, \tag{8}$$

with ρ being determined by the maximum principal plastic stretch $\bar{\lambda} = \max(\lambda_1, \lambda_2, \lambda_3)$ through $\rho = 0.85\bar{\lambda}/\sqrt{N}$, N being the average number of molecular chains between entanglements. This form expresses that the solution is in between the prediction $\boldsymbol{b}^{3-\mathrm{ch}}$ of the classical non-Gaussian three-chain rubber elasticity model [9] and the prediction $\boldsymbol{b}^{8-\mathrm{ch}}$ of the more recent eight-chain model proposed by Arruda and Boyce [14]:

$$b_\alpha^{3-\mathrm{ch}} = \tfrac{1}{3}C^{\mathrm{R}}\sqrt{N}\lambda_\alpha\mathcal{L}^{-1}\left(\frac{\lambda_\alpha}{\sqrt{N}}\right)\,, \tag{9}$$

$$b_\alpha^{8-\mathrm{ch}} = \tfrac{1}{3}C^{\mathrm{R}}\sqrt{N}\frac{{\lambda_\alpha}^2}{\lambda_{\mathrm{c}}}\mathcal{L}^{-1}\left(\frac{\lambda_{\mathrm{c}}}{\sqrt{N}}\right)\,,\quad {\lambda_{\mathrm{c}}}^2 = \tfrac{1}{3}\sum_{\beta=1}^{3}{\lambda_\beta}^2\,. \tag{10}$$

with C^{R} a statistical network parameter, and $\mathcal{L}$ the Langevin function $\mathcal{L}(\beta) = \coth\beta - 1/\beta$. Since $\mathcal{L}^{-1}(1) \to \infty$, a principal stretch equal to $\sqrt{N}$ in (9) identifies the limit stretch $\lambda_{\max}$.

The strong material rate dependence along with the intrinsic softening require due attention to the numerical implementation of the model. To improve the numerical stability, Wu and Van der Giessen [15] have developed a rate tangent formulation of the model based on the forward gradient approach proposed by Peirce *et al.* (1984). In addition it has proved convenient to use a heuristic adaptive time stepping procedure which ensures that sufficiently small steps are being taken when the material passes the yield point and starts to soften. Details on the finite element implementation used for most of the results to be presented in forthcoming sections can be found in [15].

2.2 Localization and propagation of shear bands

The strain softening after yield, eq. (6), followed by the progressing strain hardening, eqs. (8)–(10) is a key feature of plastic deformation in amorphous polymers. A typical response is shown in Fig. 1, for a set of material parameters that are characteristic for styrene-acrylonitrile (SAN): $E/s_0 = 12.6$, $\nu = 0.38$, $s_{\mathrm{ss}}/s_0 = 0.79$, $As_0/T = 52.2$, $h/s_0 = 12.6$, $\alpha = 0.25$, $N = 12.0$ and $C^R/s_0 = 0.033$, $s_0 = 120$MPa, $\dot{\gamma}_0 = 1.06 \times 10^8\,\mathrm{s}^{-1}$. It is well-known that the characteristic behaviour of softening followed by strain hardening leads to so-called *propagating instabilities* [10].

Yielding of the material tends to trigger a shear band, in which the subsequent plastic deformation concentrates. The shear strain inside this band grows until it reaches a strain (of $\Gamma \approx 1.2$ in the example of Fig. 1). Beyond that strain, the required shear stress would be larger than the

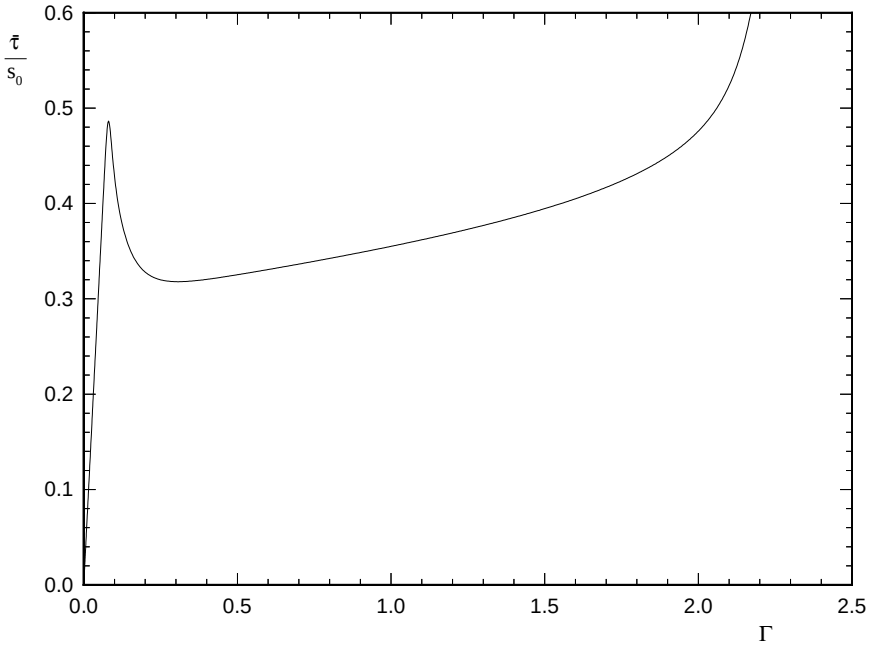

Figure 1: Shear stress ($\bar{\tau}$) response of SAN to simple shear at an applied shear rate of $\dot{\bar{\Gamma}} = 10^{-2}$ s^{-1}.

yield stress. Therefore, neighboring unyielded material will start to yield and the material in the original shear band is essentially locked. Plastic deformation thus progresses by the initiation and subsequent propagation of shear bands. A number of numerical studies [16, 17, 15] have demonstrated this in detail for elementary deformation processes as neck propagation.

From a computational point of view, it is pertinent to note that the shear bands referred to here are in fact zones of highly concentrated plastic flow; this type of localization of deformation is to be clearly distinguished from that associated with a discontinuity in shearing rate. In fact, the shearing rate inside the shear band is always limited, by virtue of the intrinsic rate-dependency of polymers through (5). This truly physical feature along with the above-mentioned limited maximum strain due to locking ensure that shear bands have a finite thickness. As long as the finite element mesh is fine enough to represent the variations across the shear band, the numerical results converge and are independent of mesh size.

3 Cohesive surface model for crazing

From a macroscopic observation, crazes and cracks are geometrically similar: both are sharp planar surfaces. However, a craze is not a crack, but consists of a web of interpenetrating voids and polymer fibrils. The fibrils are preferentially oriented normal to the craze surface, as illustrated in Fig. 2a. The fibrils bridge the craze surfaces so that load can be transmitted through the craze structure.

Crazes in amorphous polymers generally reach lengths in the order of tenths of millimeters, whereas the width of the craze remains in the order of several micrometers. When one can

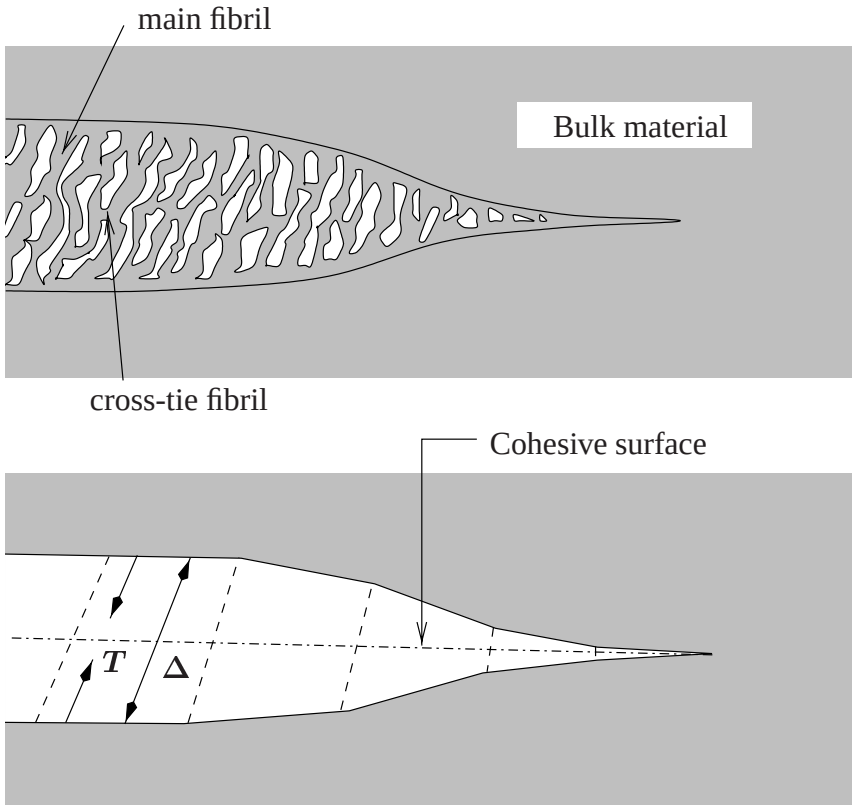

Figure 2: Schematic of modeling a craze (a) by a cohesive surface (b) characterized by a traction $\boldsymbol{T}$ and a separation $\boldsymbol{\Delta}$ over this surface.

neglect the thickness of the craze relative to the other relevant dimensions in the problem under consideration, one can replace a craze by a cohesive surface, as illustrated in Fig. 2b where the length dimension is scaled down for illustration purposes. The separation between two initially adjacent material points, one situated in the upper bulk-craze interface and the other in the bottom bulk-craze interface is described by a separation vector $\boldsymbol{\Delta}$ with normal component Δ_n and tangential component Δ_t with respect to the midplane of the cohesive surface. The traction vector $\boldsymbol{T}$ is energetically conjugate to $\boldsymbol{\Delta}$ and has components T_n and T_t. The properties of the craze matter are thus collapsed in the traction vs separation law, which will be specified below.

Multiple crazing in heterogeneous materials can be represented by embedding many potential cohesive surfaces throughout the volume, following the original ideas of Xu and Needleman [18]. The constitutive behavior of the bulk material and the craze matter are thus separated by separate constitutive laws for the cohesive surfaces and for the continuum. Crack propagation and fracture of the material as a whole then becomes independent of criteria for crack advance and only based on the micromechanical description of the crazing process.

Generally, crazing is thought to proceed in three stages (see e.g. [19]): (i) initiation, (ii) widening, (iii) breakdown of the fibrils and creation of a crack. The traction–separation law that we have developed for the cohesive zone model of a craze [4, 3] thus comprises three parts.

The physical mechanism for craze initiation is not yet clearly identified and various criteria have been proposed. From those, [4, 3] have chosen to use an empirical initiation criterion established by Sternstein and Myers [20], which is practically similar to a theoretical criterion by Argon and Hannoosh [21]. According to [20], craze initiation in a plate occurs once

$$T_n \geq \frac{3}{2}\sigma_{\rm m} - \frac{A^0}{2} + \frac{B^0}{6\sigma_{\rm m}} \tag{11}$$

with A^0 and B^0 temperature-dependent material parameters. Note the dependence on the local hydrostatic stress $\sigma_{\rm m} = \frac{1}{3}\,{\rm tr}\,\boldsymbol{\sigma}$. The criterion can be generalized to plane strain conditions by replacing the factor $3/2$ with unity [3].

Once a craze has initiated, widening of the craze ($\dot{\Delta}_n > 0$) occurs by a process of drawing-in new polymer material from the craze-bulk interface to form the highly oriented fibrils [19]. This process is accompanied by intense viscoplastic deformations in the bulk-craze interface region. Assuming that this is the rate-limiting process, we [4, 3] have argued that it can be described in a phenomenological way by a relationship between the (plastic) widening rate $\dot{\Delta}_n^c$ and the normal traction T_n that is similar to Argon's viscoplasticity law (5), i.e.

$$\dot{\Delta}_n^c = \dot{\Delta}_0 \exp\left[\frac{-A^c\sigma^c}{T}\left(1 - \frac{T_n}{\sigma^c}\right)\right], \tag{12}$$

where $\dot{\Delta}_0$ characterizes the time dependency of the craze widening process, A^c controls the temperature dependency and σ^c represents the athermal stress for craze widening. These could in principle be determined from detailed studies of craze widening at a smaller scale, but are here considered as separate material parameters.

Although crazes tend to form normal to the maximal principal stress direction, they may suffer from tangential loading at later stages of the process. As the morphology of a craze (Fig. 2a) suggests a coupling between the tangential separation and the normal separation, we propose the following viscoplastic tangential separation law, similar to (12):

$$\dot{\Delta}_t^c = \dot{\Gamma}_0 \left\{\exp\left[-\frac{A^c\tau^c}{T}\left(1 - \frac{T_t}{\tau^c}\right)\right] - \exp\left[-\frac{A^c\tau^c}{T}\left(1 + \frac{T_t}{\tau^c}\right)\right]\right\} \tag{13}$$

in which $\dot{\Gamma}_0$ and τ^c are material parameters. Note that in contrast to the normal viscoplastic widening law (12) an extra term is included that is necessary to ensure that $\dot{\Delta}_t^c$ is an odd function of T_t.

Although the ultimate breakdown of a craze is not well understood, the current viewpoint [19] seems to be that craze widening continues until the craze/bulk interface encounters a flaw sufficient for critical loss of entanglements and subsequent failure of the fibrils. A statistical description of this leads to a critical craze width, independent of the growth rate of the craze, which is consistent with many experimental observations. Within the framework of a cohesive surface model for a craze, we therefore define a critical craze width $\Delta_n^{c\,cr}$. When this limit is reached, the craze widening process ends and a microcrack is formed.

The final constitutive model for a craze is obtained by writing

$$\dot{T}_\alpha = k_\alpha(\dot{\Delta}_\alpha - \dot{\Delta}^c_\alpha)\,, \quad \alpha \in \{n, t\}\,, \tag{14}$$

where k_n and k_t are the elastic cohesive surface stiffnesses in normal and tangential direction. Prior to craze initiation, they only have a numerical significance and should have large enough values to suppress any significant opening. After craze initiation, they should represent the stiffness of the fibrillar structure [3] until the craze breaks down.

4 Numerical implementation

The numerical solution of problems of viscoplastic flow in polymers, with or without crazing by embedded cohesive surfaces, is carried out within a Total Lagrangian framework. The finite element representation is based on the rate form of the principle of virtual work,

$$\Delta t \int_V (\dot{\tau}^{ij}\delta\eta_{ij} + \tau^{ik}\dot{u}^j_{,k}\delta u_{j,i})dV + \Delta t \int_{S_i} \dot{T}_\alpha \delta\Delta_\alpha dS =$$
$$\Delta t \int_{S_u} \dot{t}^i \delta u_i dS - \left[\int_V \tau^{ij}\delta\eta_{ij}dV + \int_{S_i} T_\alpha\delta\Delta_\alpha dS - \int_{S_u} t^i\delta u_i dS\right] \tag{15}$$

in which V and S_u are the volume and outer surface of the body in the reference configuration. The τ^{ij} are the components of the second Piola-Kirchhoff stress tensor and T^i are the corresponding traction vector components; the components of the dual Lagrangian strain-rate tensor are $\dot{\eta}_{ij}$.

The S_i in (15) denotes the collection of all cohesive surfaces contained in V. They may be confined to a single surface in the material (if the craze location is known *a priori*, as in Sec. 6) or may be scattered over the entire volume (as in the example of Sec. 5). In the latter case we use linear triangular elements to discretize the continuum with cohesive surface elements as interface elements between adjacent elements. In applications with a single cohesive surface (Sec. 5) we use quadrilateral elements for the continuum, each element being built-up by four crossed triangles.

The term in (15) between square brackets is the equilibrium correction which is zero for a state of perfect equilibrium. This term is included to prevent drifting of the solution from the true equilibrium path due to the finite time increments. The finite element equations are obtained by eliminating the stress rates $\dot{\tau}^{ij}$ using the continuum constitutive equations (1)–(10) and eliminating the cohesive surface traction rates using (12)–(14). The numerical integration of the stiffness contributions of the cohesive surface elements is carried out with Newton-Cotes integration.

5 Crazing vs plasticity near crack tips

Simple pictures of failure of polymers consider crazing and shear yielding as two independent mechanisms, and classify failure as being either brittle due to crazing or ductile due to shear yielding. Detailed experiments by Ishikawa and co-workers [22, 23] however have shown that

crazing can occur subsequent to shear yielding in materials such as PC and PMMA. Also in polymer-rubber blends, such as acrylonitrile-butadiene-styrene (ABS), crazing and shear yielding can occur simultaneously.

In order to develop a basic understanding of this, we [3] recently performed a study of the interaction between plasticity and crazing near crack tips under plane strain, mode I conditions. This work continues from a numerical analysis of the near-tip fields caused by shear yielding only [24]. In the latter it has been shown that the crack-tip fields are quite different from the HRR fields developed for metals which were often just assumed to hold for polymers as well (see, e.g., [1]). The underlying reason for this is the characteristic softening and re-hardening of amorphous polymers seen in Fig. 1, which gives rise to localized plastic deformations in the form of shear bands that propagate as the load continues to increase.

Using the material parameters for viscoplasticity in SAN mentioned in Sec. 2.2, this shear banding is demonstrated in Fig. 3a. This figure shows the distribution of the instantaneous plastic shear rate in the region around the tip of a blunted crack (tip radius $r_t = 0.1$ mm). The calculation was carried out under the assumption of small-scale yielding, with the boundary conditions on a circular arc of radius $200r_t$ according to the elastic mode I crack tip field. The stress intensity factor is applied from stress-free initial conditions at a constant loading rate $\dot{K}_I$. At the particular loading shown in Fig. 3a, the current plastic activity takes place in a number of shear bands that emanate from the free notch surface.

Figure 3b now shows the situation at the same applied stress intensity factor when crazing is accounted for by means of a cohesive surface laid out in front of the crack. The material parameters assumed for the crazing model are $A^0 = 82$ MPa, $B^0 = 20000$ MPa^2, $A^c = 400$ K/MPa, $\Delta_n^{c,cr} = 10$ μm, $\dot{\Delta}_0 = 10$ mm/s and $\sigma_c = 100$ MPa ($T = 293$ K). For this case, the craze initiated at the root of the notch and quickly propagated forward. Notice that the development of the craze has reduced the amount of plastic deformation necessary to accommodate the same applied stress intensity factor as in Fig. 3a. The instant shown in Fig. 3b is chosen because this is when the first breakdown of crazes is taking place. Once this has happened, a crack is quickly formed inside the craze and rapid crack propagation takes place, so that the load at this stage can be considered as the critical stress intensity factor. As one can see from the craze profile, craze breakdown in this case occurs at the point where the currently most active shear bands intersect, thus providing an example of how the interaction or competition between shear yielding and crazing can take place.

The detailed parameter study in [3] has demonstrated that this competition can emerge in various forms depending on loading rate and temperature. An example of this is given in Fig. 4, which shows similar results but at a 120 times higher applied loading rate $\dot{K}_I$. In the absence of crazing, Fig. 4a, shear banding is more localized than in Fig. 3a. This can be understood from the fact that a higher deformation rate would require higher stresses for accommodation by viscoplasticity to be possible; hence, plasticity is somewhat suppressed. This also occurs in the presence of crazing, but then there is also a rate dependency of the widening of the craze, since this also occurs by a viscous process, Eq. (12). As a consequence of both effects, we observe significantly less plastic activity in Fig. 4b than at the lower loading rate of Fig. 3b. This also affects the profile of the craze. In fact, also this situation corresponds to the instant of first

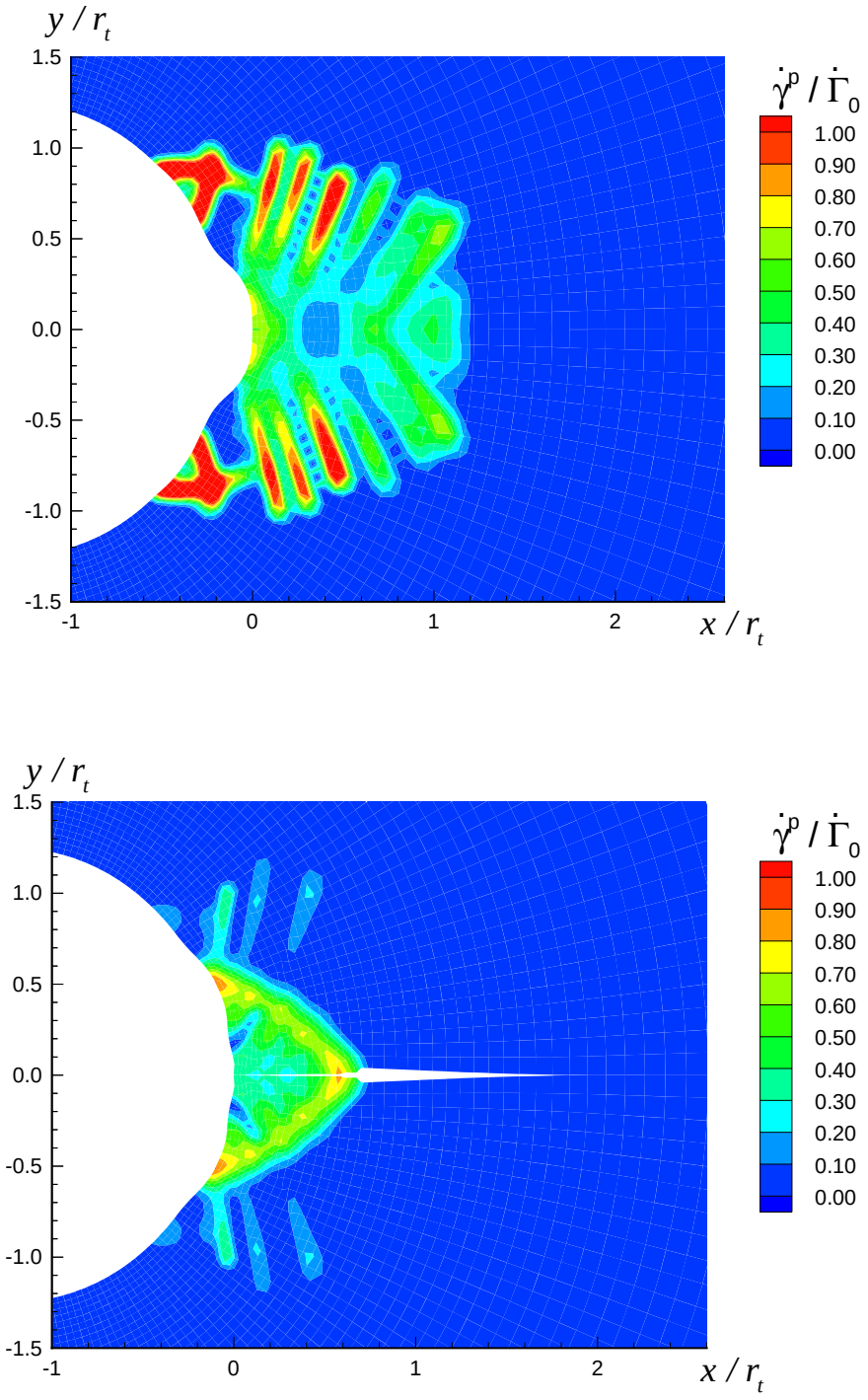

Figure 3: Distribution of instantaneous plastic shear rate $\dot{\gamma}^{\mathrm{p}}$ near notch tip in SAN under mode I loading at $\dot{K}_I \approx 3.10^{-2}\,\mathrm{MPa}\sqrt{\mathrm{m}}/\mathrm{sec}$ when $K_I/(s_0 r_t) \approx 1.71$, (a) without accounting for crazing; (b) with crazing.

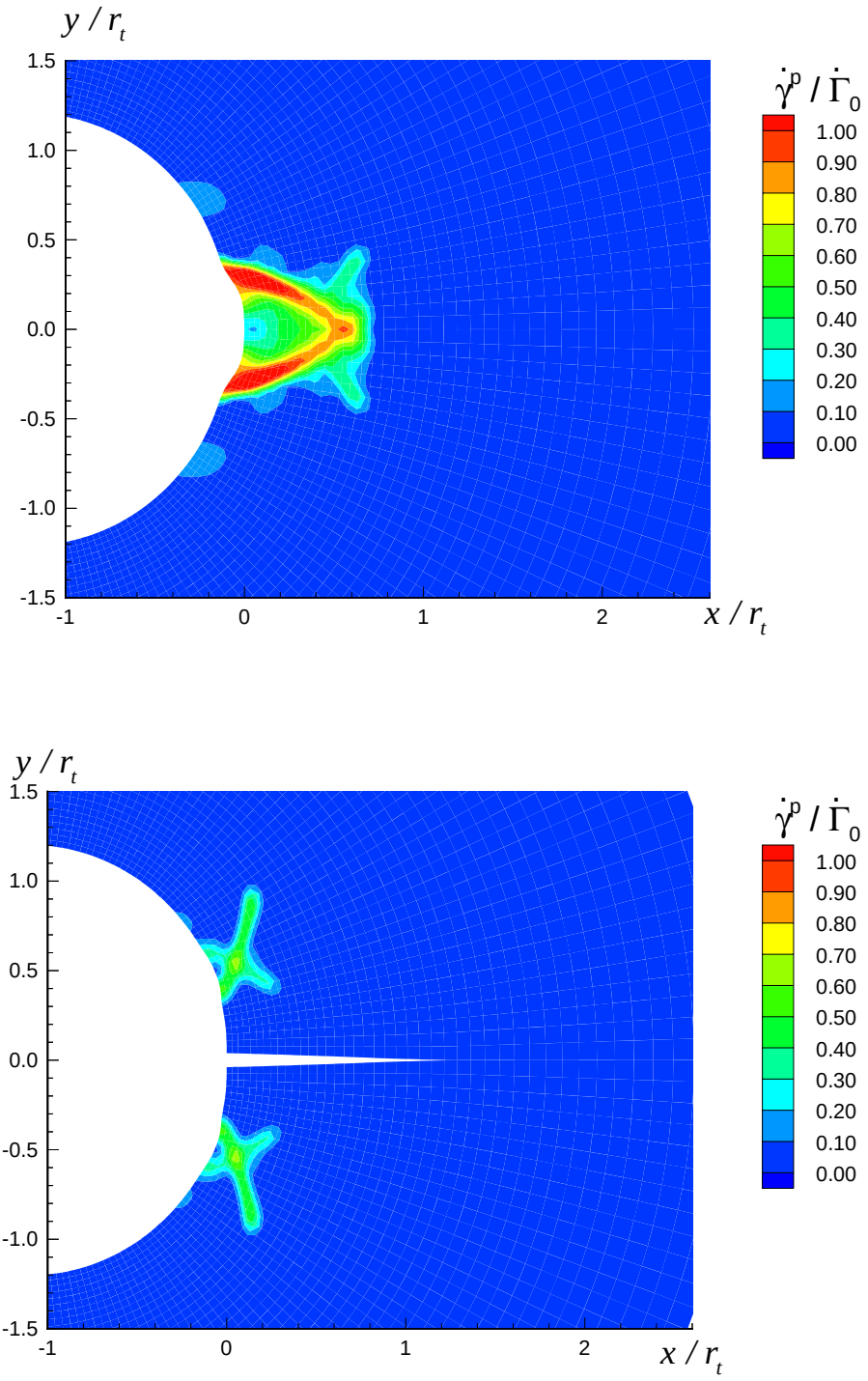

Figure 4: Distribution of instantaneous plastic shear rate $\dot{\gamma}^{\mathrm{p}}$ near notch tip in SAN under mode I loading at a rate that is 120 times larger than in Fig. 3 when $K_I/(s_0 r_t) \approx 1.56$, (a) without accounting for crazing; (b) with crazing.

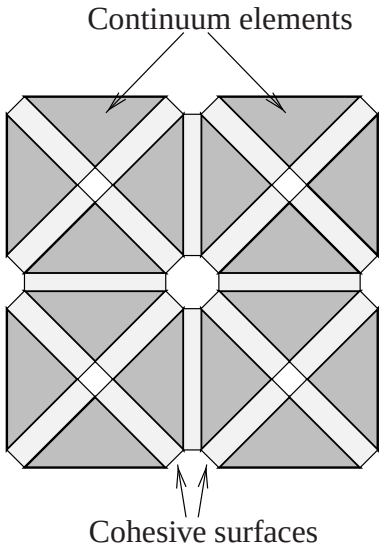

Figure 5: Illustration of the arrangement of continuum elements and embedded cohesive surfaces.

fibril breakdown in the craze, but in this case it occurs at the tip of the notch. The corresponding critical stress intensity factor is reduced relative to the lower loading rate shown in Fig. 3b.

6 Multiple crazing around notches

The original experiment that led Sternstein and Meyers [20] to their craze initiation criterion (11) was on a PMMA plate with a central hole loaded in uniaxial tension. After load application, zones with a high density of crazes around the hole were observed. From the size of these zones, (11) was deduced.

Tijssens *et al.* [4] simulated this experiment, by application of the embedded cohesive surface methodology. Within wedge shaped regions of 45° above and below the equatorial plane of the hole, cohesive surface elements are immersed between all triangular continuum elements (see Fig. 5). No viscoplasticity is accounted in the analysis, and the elastic properties are taken to be $E = 3240$ MPa and $\nu = 0.35$. The material parameters for the crazing model are $A^0 = 42$ MPa, $B^0 = 3000$ MPa^2 ($T = 313$ K), $A^c = 100$ K/MPa, $\Delta_n^{c,cr} = 2.7\ \mu$m, $\dot{\Delta}_0 = 10$ mm/s and $\sigma_c = 60$ MPa. Just as in [20], the dimensions of the plate are $2 \times 1/2$ inch with a hole of diameter $1/16$ inch.

Figure 6 shows the stress distribution after loading at a remote stress rate of 5.52 MPa/s up to 16 MPa. Craze initiation has started obviously at the elastic stress concentration at the equator of the hole. While the early crazes propagated laterally into the plate, the craze zone also expanded in the direction of loading. No breakdown of the crazes has taken place yet at the instant shown, so that the crazes still transmit stresses while they widen according to (12). The overall load versus displacement curve showed no deviation from the perfectly elastic response. As the

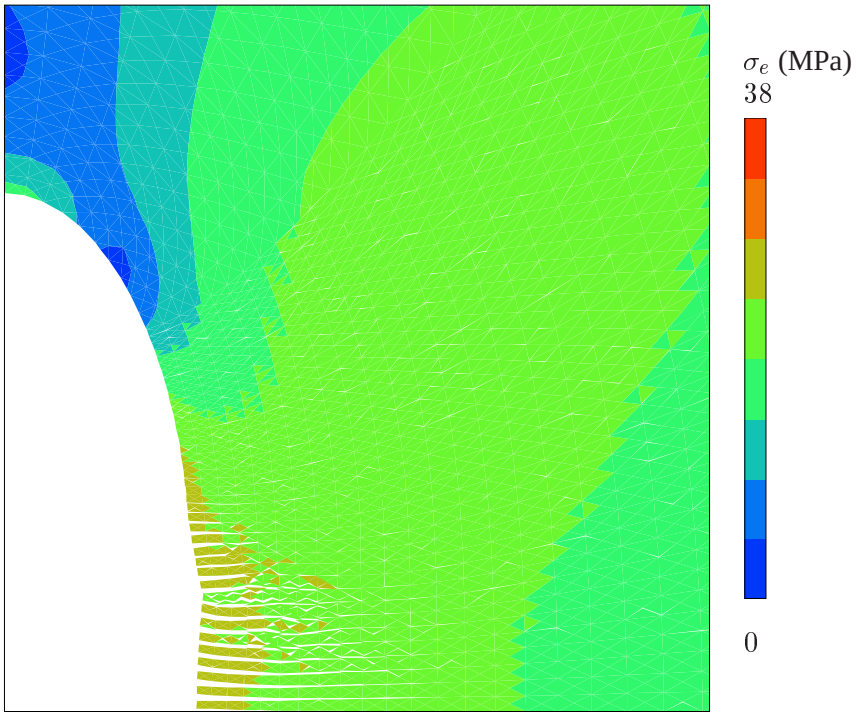

Figure 6: Craze zone and effective stress distribution around a hole in a PMMA plate at a global stress level of 16 MPa in the vertical direction at $T = 313$ K. The displacements are multiplied by a factor of 20 to visualize the crazes, i.e. the white fringes near the equator.

applied load increases beyond the value shown in Fig. 6, the craze zone further expands and the stress redistributions away from the elastic solution become more significant [4].

Mesh sensitivity studies were carried out [4] to show that mesh refinement leads to a converged craze zone development with increasing load. As the crazes line up with the element boundaries, see Fig. 6, there will be dependence on the mesh orientation however.

7 Failure mechanisms in polymer-rubber blends

It is a well established fact that the fracture toughness of polymers can be greatly enhanced by adding a dispersion of rubber particles, of typically between 20 and 40vol. %. The toughening is commonly assumed to involve a number of mechanisms: crazing, cavitation and shear yielding (see, e.g., [5]). Cavitation of the rubber particles relieves the stress triaxiality in the matrix polymer. This suppresses the likelihood of matrix crazing and promotes plastic deformation in the matrix by shear yielding. The toughening effect is generally enhanced when a region of large plastic deformation spreads out over a large volume in the material.

Toughening in blends involves a range of length scales. The ‘macroscopic scale’ is the scale at which plastic deformation and crazing take place in the neighborhood of a propagating crack in a blend. The next smaller, ‘mesoscopic’ scale is the size scale at which the individual rubber

particles can be distinguished. This is a crucial scale for our understanding of toughening in blends since it is at this size scale that rubber cavitation, crazing and shear yielding compete with each other and determine which one(s) of them dominate(s).

In a series of papers, Steenbrink *et al.* and Pijnenburg *et al.* (e.g. [6, 7, 8, 25]) investigated some basic issues at this scale related to cavitation and plastic flow around cavitated particles. The interest here is mainly directed towards ABS blends, consisting of an SAN matrix and polybutadiene rubber particles. Basically, these are studies for blends with periodic arrays of particles so that the computations can be carried out for a unit cell containing a single rubber particle. Moreover, it was shown in [7] that once the rubber particle has cavitated internally, it is mechanically equivalent to a void for realistic rubber properties. Three-dimensional models have been used for spherical rubber particles under axisymmetric stressing, but also planar studies have been performed. Planar computations allow for unit cell and associated boundary conditions that are less constrained than axisymmetric ones.

Figure 7 shows a typical result of such cell calculations under axisymmetric conditions. The rubber particle has been assumed to have cavitated, leaving a void with initial radius a_0 and half-spacing b_0 of $a_0/b_0 = 0.5$ (corresponding to a particle/void volume fraction of $f_0 = 0.083$). The material parameters for the SAN matrix are the same as mentioned in Sec. 2.2 and used in the Sec. 5. The overall, macroscopic loading is applied under strain control, with all cell boundaries remaining straight. Loading is primarily in the x_2 direction, but is applied such that the macroscopic stress triaxiality (overall hydrostatic stress Σ_{m} relative to effective Mises stress Σ_{e}) remains constant. The results in Fig. 7 are typical for many other materials studied [6, 7]. Local plastic deformation starts from the equator of the void. At sufficiently low triaxiality, as is the case here, plasticity initiates in the form of shear bands at about 45° to the principal loading direction (Fig. 7a). With increased overall loading, these shear bands propagate, until macroscopic yield occurs. Just as in the local response, the overall behavior then shows softening which is due to the formation of a different type of shear bands, as shown in Fig. 7b. This type has been referred to as 'dog-ear' shear bands in [7] and is found to be present from the beginning under higher stress triaxiality. The main characteristic of the shear bands formed at macroscopic yield is that they connect two neighboring voids. As macroscopic straining continues, these bands propagate as well, leading essentially to necking and neck propagation of the ligament between voids (Fig. 7c).

An important drawback of these kind of cell analyses is that their symmetries imply rather strong constraints on the local deformation. Since polymers have the tendency to deform plasticity by propagating shear bands, such constraints may suppress localized modes that would form in realistic systems [26]. Therefore, we recently carried out cell analyses [25] in which the symmetries in loading are removed and the kinematic boundary conditions are replaced by the more general periodic boundary conditions. Figure 8 shows how plastic deformation then progresses under macroscopic simple shear. In this case the model is a planar one, with cylindrical voids but the same ratio $a_0/b_0 = 0.5$ as in Fig. 7 (yet a different volume fraction of $f_0 = 0.2$). Prior to macroscopic yield, Fig. 8a, dog-ear shear bands are formed normal to the principal tensile stress direction (which is roughly at 45° to the shear direction). At macroscopic yield (Fig. 8b), new shear bands are formed which link up adjacent voids in the shear direction. Upon

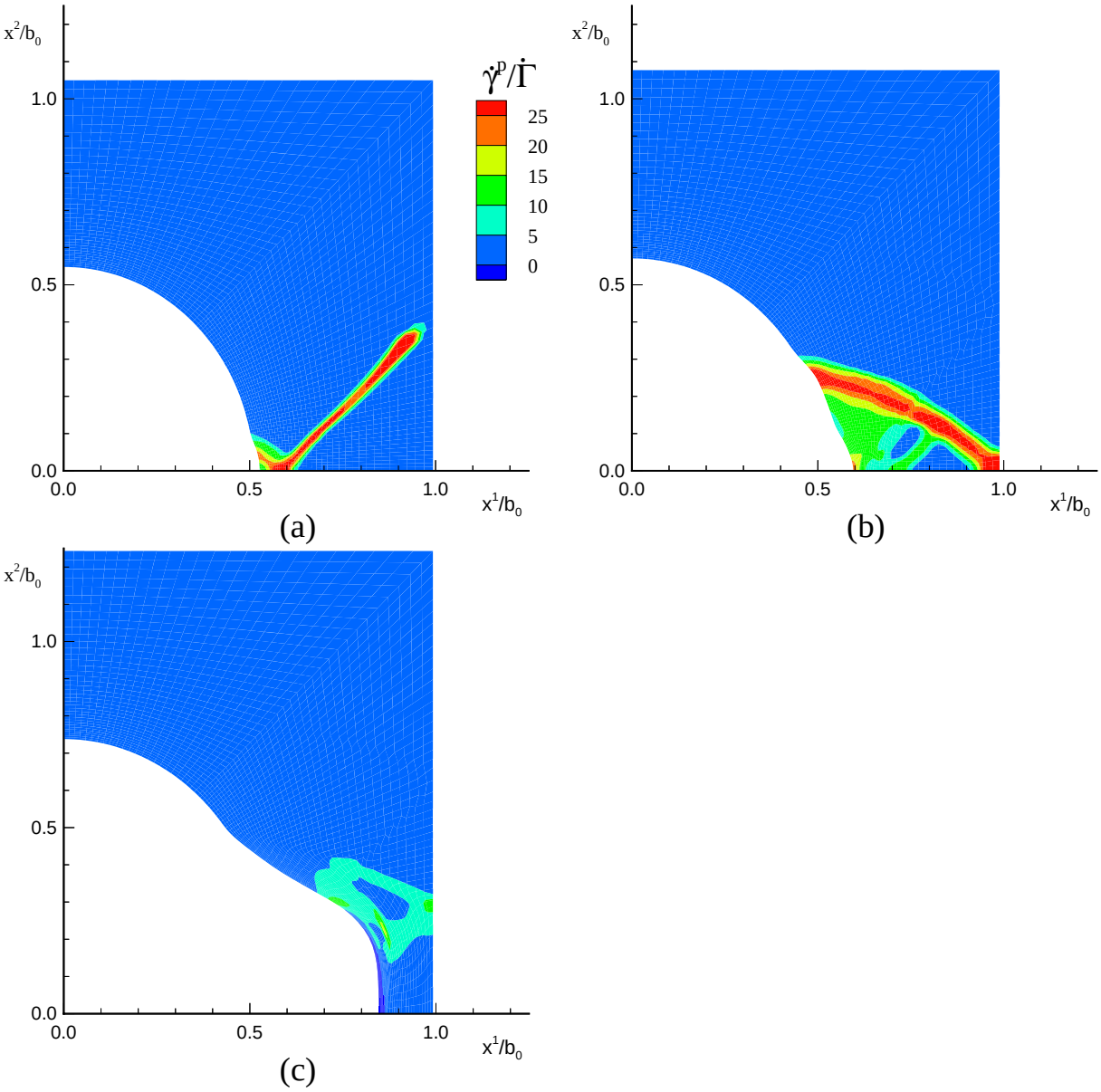

Figure 7: Distribution of instantaneous plastic shear rate near a spherical void in a SAN matrix under a macroscopic stress triaxiality of $\Sigma_m/\Sigma_e = 1$ at three stages of deformation: (a) just prior to macroscopic yield; (b) just after yield; (c) after continued macroscopic straining.

continued macroscopic shearing, these shear bands widen by propagation of the active shear regions through the same mechanism as discussed previously (Fig. 8c).

It is noted that the deformed void (or particle) shape that develops under macroscopic shear is quite different from that under predominant tension. Under tension, Fig. 7c, we observe a significant increase of the volume of the void with a somewhat bulgy surface. Although the details in a random stacking of particles will be different, there is some qualitative correspondence with the shapes of cavitated rubber particles found ahead or at some distance from cracks in ABS experimentally. The S-like void shape found under simple shear, Fig. 8c, is also found experimentally, but only quite near and below the fracture surface. We have conjectured in [8] that

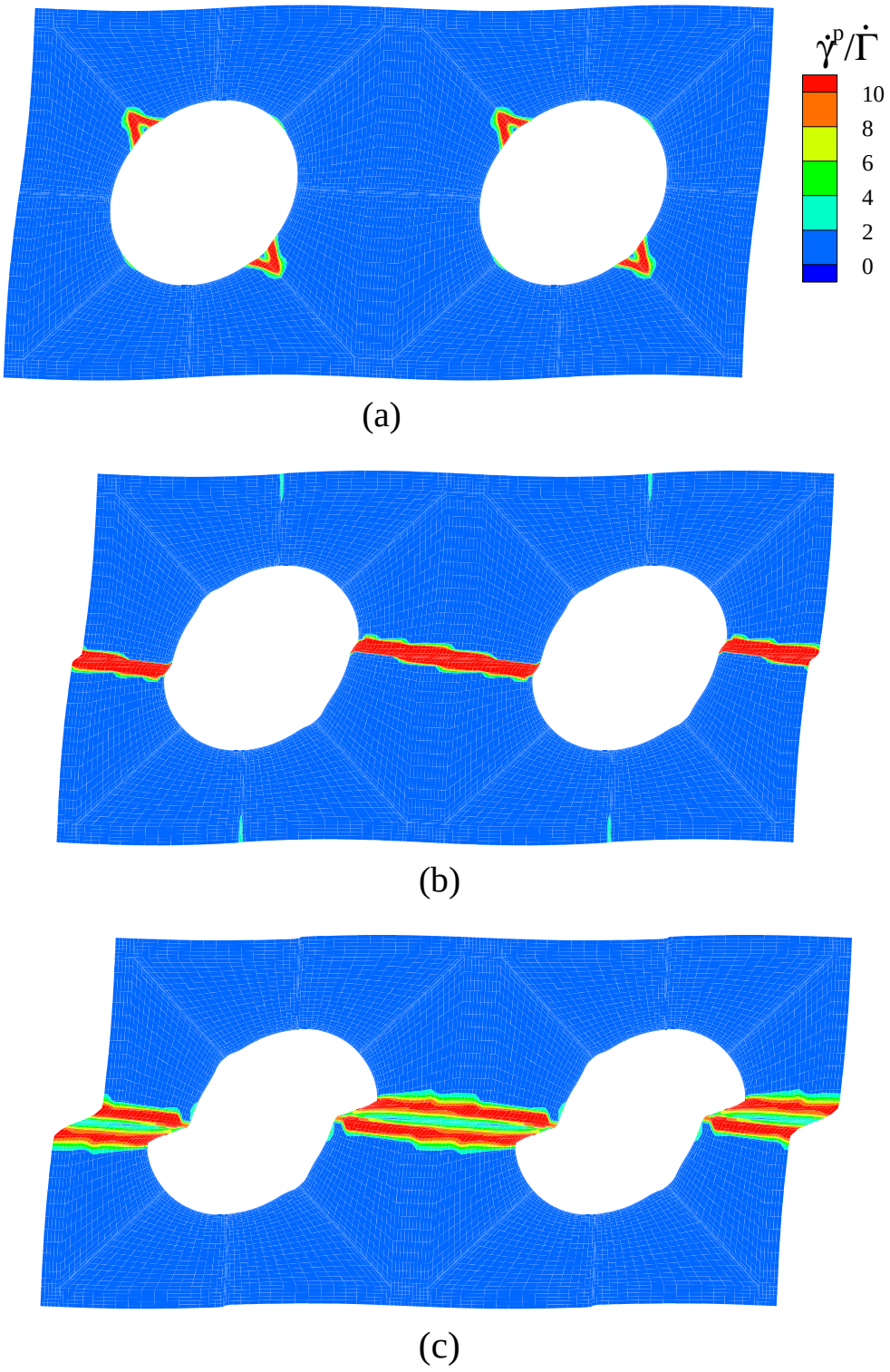

Figure 8: Distribution of instantaneous plastic shear rate near a cylindrical void in a SAN matrix under macroscopic simple shear at three stages of deformation: (a) prior to macroscopic yield; (b) just after yield; (c) after continued macroscopic straining.

this indicates that shearing takes place in the blend at a macroscopic level while a crack moves by. Ahead of the crack tip, high triaxial tension is apparently dominant, while shearing occurs in the wake. This would have important consequences for the understanding of how toughening by the rubber particles takes place. This is the subject of continued research.

8 Conclusions

The examples of recent computational studies given in this paper serve to demonstrate that plasticity and fracture in polymeric systems have particular features that distinguish them from those in metals. Both in plasticity and fracture, the physical mechanisms involve localization. Plasticity, or shear yielding, leads to the initiation and propagation of shear bands, which are a consequence of intrinsic softening after yield followed by orientational hardening. Fracture is commonly caused by crazing, which involves localization of deformation in the craze, which widens because of local plastic flow at a very small size scale.

The development of a constitutive model for plasticity and a cohesive surface model for crazing that capture these essential features has taken place quite recently. This is especially true when compared to the time frame over which metal plasticity and fracture have been studied. Thus, there are still many open issues in polymer fracture — there is much that computational mechanics can contribute to help resolve them.

References

[1] J.G. Williams: *Fracture Mechanics of Polymers*, Ellis Horwood, Chichester (1984).

[2] P.D. Wu and E. Van der Giessen: *On improved network models for rubber elasticity and their applications to orientation hardening in glassy polymers.* J. Mech. Phys. Solids, **41**, (1993), 427–456.

[3] R. Estevez, M.G.A. Tijssens and E. Van der Giessen: *Modeling of the competition between shear yielding and crazing in glassy polymers.* in preparation.

[4] M.G.A. Tijssens, E. Van der Giessen and L.J. Sluys: *Modeling of crazing using a cohesive surface methodology.* submitted to Mech. Mater.

[5] C.B. Bucknall: *Toughened Plastics.* Applied Science Publ., London, (1977), 177–179.

[6] A.C. Steenbrink, E. van der Giessen and P.D. Wu: *Void growth in glassy polymers.* J. Mech. Phys. Solids, **45**, (1997), 405–437.

[7] A.C. Steenbrink and E. van der Giessen: *On cavitation, post-cavitation and yield in amorphous polymer-rubber blends.* J. Mech. Phys. Solids, **47**, (1999), 843–876.

[8] K.G.W. Pijnenburg, A.C. Steenbrink and E. van der Giessen: *Shearing of particles during crack growth in polymer blends.* Polymer (in press).

[9] M.C. Boyce, D.M. Parks and A.S. Argon: *Large inelastic deformation of glassy polymers, Part I: rate dependent constitutive model.* Mech. Mater., **7**, (1988), 15–33.

[10] E. van der Giessen: *Localized Plastic Deformations in Glassy Polymers.* Eur. J. Mech. A/Solids, **16**, (1997), 87–106.

[11] A.S. Argon: *A theory for the low-temperature plastic deformation of glassy polymers.* Phil. Mag., **28**, (1973), 839–865.

[12] E.M. Arruda, M.C. Boyce and R. Jayachandran: *Effects of strain rate, temperature and thermomechanical coupling on the finite strain deformation of glassy polymers.* Mech. Mater., **19**, (1995), 193–212.

[13] L.R.G. Treloar: *Physics of Rubber Elasticity.* Oxford Univ. Press, 3rd edn. (1975).

[14] E.M. Arruda and M.C. Boyce: *A three-dimensional constitutive model for large stretch behaviour of rubber materials.* J. Mech. Phys. Solids, **41**, (1993), 389–412.

[15] P.D. Wu and E. Van der Giessen: *Computational aspects of localized deformations in amorphous glassy polymers.* Eur. J. Mech., A/Solids, **15**, (1996), 799–823.

[16] P.D. Wu and E. Van der Giessen: *Analysis of shear band propagation in amorphous glassy polymers.* Int. J. Solids Structures, **31**, (1994), 1493–1517.

[17] P.D. Wu and E. Van der Giessen: *On neck propagation in amorphous glassy polymers under plane strain tension.* Int. J. Plasticity, **11**, (1995), 211–235.

[18] X.-P. Xu and A. Needleman: *Numerical Simulations of Fast Crack Growth in Brittle Solids.* J. Mech. Phys. Solids, **42**, (1994), 1397–1434.

[19] H.H. Kramer and L.L. Berger: *Fundamental Processes of Craze Growth and Fracture.* Adv. Polym. Sc., **91/92**, (1990), 1–68.

[20] S.S. Sternstein and F.A Myers: *Yielding of Glassy Polymers in the Second Quadrant of Principal Stress Space.* J. Macromol. Sci.-Phys., **B8**, (1973), 539–571.

[21] A.S. Argon and J.G. Hannoosh: *Initiation of crazes in polystyrene.* Phil. Mag., **36**, (1977), 1195–1216.

[22] M. Ishikawa, I. Narisawa and H. Ogawa: *Criterion for craze nucleation in polycarbonate.* J. of Polymer Sci., **15**, (1977), 1791–1804.

[23] M. Ishikawa and H. Ogawa: *Brittle fracture in glassy polymers.* J. Macromol. Sci.-Phys., **19**, (1981), 421–443.

[24] J. Lai and E. Van der Giessen: *A numerical study of crack-tip plasticity in glassy polymers.* Mech. Mater., **25**, (1997), 183–197.

[25] K.G.W. Pijnenburg and E. Van der Giessen: *Macroscopic yield in cavitated polymer blends*. submitted to Int. J. Solids Struct.

[26] R.J.M. Smit, W.A.M. Brekelmans and H.E.H. Meijer: *Prediction of the large-strain mechanical response of heterogeneous polymer systems: local and global deformation behaviour of a representative volume element of voided polycarbonate.* J. Mech. Phys. Solids, **47**, (1999), 201–221.